RESEARCH ARTICLE

Check for updates

An organic–inorganic hybrid polyoxoniobate decorated by a Co(III)-amine complex for electrocatalytic urea splitting†

Da-Huan Li, Nian Shi, Yong-Jiang Wang, Ping-Wei Cai, [ID] Yan-Qiong Sun [ID] * and Shou-Tian Zheng [ID] *

The overall energy efficiency of electrochemical systems is significantly reduced by the conventional anodic oxygen evolution reaction (OER). It is feasible to improve energy efficiency by replacing the OER with the urea oxidation reaction (UOR), which has a lower thermodynamic potential. An organic–inorganic hybrid polyoxoniobate decorated by a Co(III)-amine complex, $Na_4(H_2O)_{15}[Co(en)_3]_2\{[Co(en)(Nb_6O_{19})]_2\}\cdot34H_2O$ (**Co₂Nb₆**, en = ethylenediamine) with distinct physicochemical characteristics and well-defined single-crystal structure is reported. The structure of **Co₂Nb₆** contains Lindqvist $\{[Co(en)(Nb_6O_{19})]_2\}^{10-}$ dimer and free $[Co(en)_3]^{3+}$ complexes. **Co₂Nb₆** exhibits remarkable catalytic activity for the UOR after being firmly attached to the surface of acetylene black by polyethyleneimine (PEI). To the best of our knowledge, this is the first instance of performing the electrocatalytic UOR based on Lindqvist polyoxoniobate clusters, which will pave the path for innovative concepts in the development of POM-based electrocatalysts.

Introduction

In recent years, global attention has been drawn to the growing challenges of energy and environment.[1] One promising solution to these challenges is hydrogen, which offers high eco-friendliness, energy density, calorific value, and intermittent availability among renewable resources.[2] Electrocatalytic oxidation is a critical process for addressing environmental issues.[3] The urea oxidation reaction (UOR) serves as a potential solution to purify urea-rich wastewater while generating hydrogen.[4] It's worth noting that the cell potential required for urea electrolysis is theoretically much lower than that required for water electrolysis.[5] In addition, the UOR is a key chemical process in artificial kidneys and direct urea fuel cells.[6] However, the UOR has slow kinetics due to its complex intermediate transfers, $6e^-$ transfer process, and multiple gas-desorption steps.[7] So far, precious metal-based catalysts, such as Pt, IrO_2, and RuO_2, have been proven to exhibit high catalytic activity for the UOR, similar to those used in the hydrogen

evolution reaction (HER) and the oxygen evolution reaction (OER).[8–10] Nevertheless, their high cost, scarcity, and poor stability limit their large-scale applications.[11] Therefore, there is a need to design and develop alternative catalysts with enhanced activity and lower cost for efficient hydrogen production by the UOR.

Recently, a variety of highly efficient catalysts for the UOR have been developed, including non-noble metal oxides, sulfides, phosphides, hydroxides, and nitrides.[12–16] However, the interfacial information of these nanocatalysts is often complex, posing challenges to establishing a solid structure–property-performance relationship of the catalysts.[17] Furthermore, the aggregation of active sites in the catalysts can lead to reduced catalytic activity.[18] As a result, creating a structurally stable precursor at the molecular level using the grafting method to efficiently disperse catalytically active sites has become a significant challenge for electrocatalysis.[19] Based on this design concept, it is believed that crystalline catalysts with clear structures could provide an opportunity where this concept is put into practice and extend the possibilities of efficient hydrogen production.

Polyoxoniobates (PONbs), a subset of polyoxometalates, are a promising class of electrocatalytic nanomaterials due to their precise architecture and highly charged negative surface.[20,21] Specifically, the Lindqvist-type $[Nb_6O_{19}]^{8-}$ cluster not only accelerates surface charge transport as a co-electron group but also maintains structural stability under strongly alkaline con-

College of Chemistry, Fuzhou University, Fuzhou, Fujian 350108, People's Republic of China. E-mail: sunyq@fzu.edu.cn, stzheng@fzu.edu.cn; Fax: +86-591-22866340

This journal is © the Partner Organisations 2023

Inorg. Chem. Front., 2023, **10**, 4789–4796 | **4789**

ditions with a pH value of 14, making it a potential electrocatalytic carrier under alkaline conditions.[22] In addition, it can serve as an excellent O donor to bond transition metal (TM) ions.[23] However, TM ions tend to form suspended hydroxide that precipitates in alkaline media.[24,25] To address this issue, N-donor organic ligands are chosen to chelate with TM cations to produce TM-organic complexes, which can subsequently recombine with $[Nb_6O_{19}]^{8-}$ clusters as a structural linker and modulator to establish charge homeostasis.[26] Furthermore, the $[Nb_6O_{19}]^{8-}$ cluster plays a crucial role in dispersing TM-organic complexes, which can ultimately form stable organic–inorganic hybrid TM-PONbs.[27]

It is well known that the catalytic activity of clusters is highly susceptible to their low stability in water or under reaction conditions.[28] Due to their strong adhesion to the electrode surface, the bubbles produced during the gas reaction tend to accelerate the detachment of active chemicals from the electrode surface, making it difficult to achieve high catalytic activity.[29–31] In order to improve the catalytic activity of clusters, grafting metal complexes onto polyoxometalates (POMs) at the molecular level has been proposed as an effective alternative. This approach improves the mechanical stability of associated metal complexes and the electron transfer rate, as the covalent bonds attached to POMs enhance the stability of POMs.[32–34] For instance, Gong used the cationic polymer polyethyleneimine (PEI) to immobilize Co_4POM on commercial TiO_2 nanoparticles, which demonstrated that highly reactive cobalt oxide is the main activity center of the OER.[25] Despite being promising electrocatalysts, polyoxometalates containing cobalt complexes have not yet been reported to electrocatalytically oxidize urea.[35]

In this study, a polyoxoniobate decorated by a Co(III)-amine complex, $Na_4(H_2O)_{15}[Co(en)_3]_2\{[Co(en)(Nb_6O_{19})]_2\}\cdot34H_2O$ (**Co$_2$Nb$_6$**, en = ethylenediamine), has been constructed from $\{[Co(en)(Nb_6O_{19})]_2\}^{10-}$ dimers and $[Co(en)_3]^{3+}$ complexes. The strong adsorption ability of PEI was employed to anchor **Co$_2$Nb$_6$** onto acetylene black (**AB**) as a UOR catalyst (**Co$_2$Nb$_6$&AB**). PEI was used to effectively reduce the adhesion of air bubbles on the catalyst surface, while acetylene black acted as a conductive substrate to enhance the catalytic activity of POMs by compensating for their weak conductivity. Due to the PONb clusters effectively partitioning the Co^{3+} active sites, **Co$_2$Nb$_6$&AB** shows excellent UOR catalytic activity and stability in alkaline electrolytes. Furthermore, our research highlights the advantages of creating crystal structures with well-defined electrocatalytic active sites.

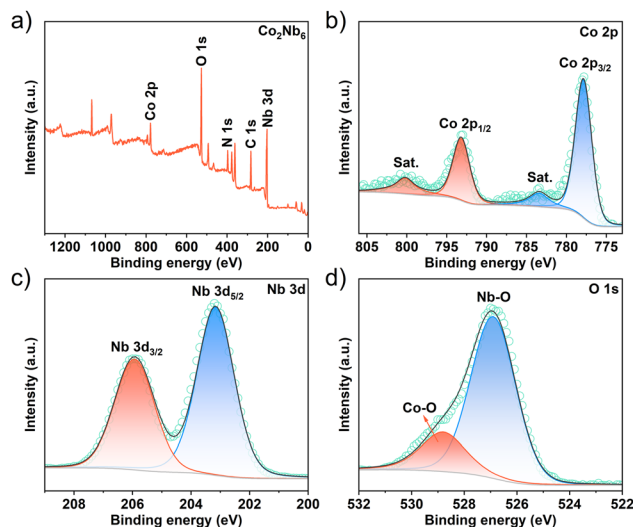## Results and discussion

Crystal structure of Co$_2$Nb$_6$

The compound **Co$_2$Nb$_6$** displays a one-dimensional organic–inorganic hybrid chain structure. X-ray single-crystal diffraction shows that compound **Co$_2$Nb$_6$** crystallizes in the triclinic $P\bar{1}$ space group and contains $\{[Co(en)(Nb_6O_{19})]_2\}^{10-}$ dimers and $[Co(en)_3]^{3+}$ units. The crystal data and structure refinement are

listed in Table S1.† Valence bond calculations show that Nb and Co atoms possess +5 and +3 valences, respectively (Table S2†). Two centrosymmetric $[Nb_6O_{19}]^{8-}$ clusters are linked by two centrosymmetric $[Co(en)]^{3+}$ units to form a cyclic $\{[Co(en)(Nb_6O_{19})]_2\}^{10-}$ dimer (Fig. 1a). The $[Co(en)]^{3+}$ complexes are grafted onto the $[Nb_6O_{19}]^{8-}$ clusters because Co^{3+} adopts a six-coordinated octahedral environment with four oxygen atoms from two $[Nb_6O_{19}]^{8-}$ clusters and two nitrogen atoms from one en ligand (Fig. 1a). This is helpful for increasing the catalytic activity. Two different kinds of $\{[Co(en)(Nb_6O_{19})]_2\}^{10-}$ secondary building units exist in **Co$_2$Nb$_6$**. One of these is further linked by Na^+ to create a one-dimensional zigzag chain structure running along the b axis (Fig. 1c), while the other is discrete and surrounded by two "V"-shaped $\{Na_3(H_2O)_{13}\}$ clusters and eight $[Co(en)_3]^{3+}$ cations. The isolated $\{[Co(en)(Nb_6O_{19})]_2\}^{10-}$ is located in the center of the regular parallelepiped formed by eight $[Co(en)_3]^{3+}$ cations. In the packing structure (Fig. 1b), the 1D zigzag chains are arranged in parallel along the [100] direction in the –AAAA– sequence and the isolated $\{[Co(en)(Nb_6O_{19})]_2\}^{10-}$ and $[Co(en)_3]^{3+}$ are distributed between the chains (Fig. 1d).

The electronic interactions of surface elements in **Co$_2$Nb$_6$** were investigated using X-ray photoelectron spectroscopy (XPS). The XPS survey spectra reveal the presence of Co, O, Nb, N, and C elements in **Co$_2$Nb$_6$**, as demonstrated in Fig. 2a. The Co 2p spectrum consists of two spin–orbit doublets and two satellite peaks, with binding energy values of 777.9 and 793.2
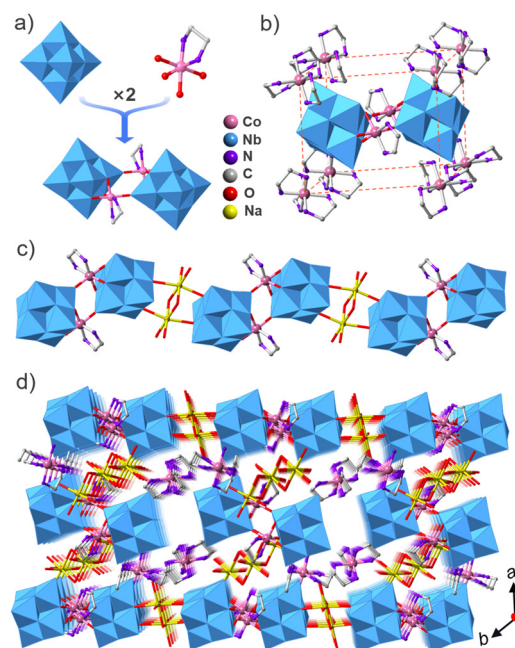

Fig. 1 (a) The structure of the $\{[Co(en)(Nb_6O_{19})]_2\}^{10-}$ dimer; (b) view of the regular parallelepiped formed by eight $[Co(en)_3]^{3+}$ cations that encircle the $\{[Co(en)(Nb_6O_{19})]_2\}^{10-}$ dimer; (c) view of the 1D zigzag chain structure constructed from the $\{[Co(en)(Nb_6O_{19})]_2\}^{10-}$ dimer and Na^+ cations in **Co$_2$Nb$_6$**; and (d) view of the packing structure of **Co$_2$Nb$_6$**. Atomic color code: Co, pink; O, red; Nb, blue; N, purple; C, grey; Na, yellow; polyhedral color code: NbO_6, blue.

4790 | *Inorg. Chem. Front.*, 2023, **10**, 4789–4796

This journal is © the Partner Organisations 2023

Inorganic Chemistry Frontiers   Research Article

Fig. 2 XPS spectra of Co_2Nb_6. (a) survey spectrum; (b) XPS spectrum of Co 2p; (c) XPS spectrum of Nb 3d; and (d) XPS spectrum of O 1s.

eV observed for Co $2p_{3/2}$ and Co $2p_{1/2}$ (Fig. 2b), respectively. These results suggest the presence of the cobalt ion in its highest oxidation state, *i.e.*, Co^{3+}.[36,37] The presence of Co^{3+} can generate more reactive intermediates (CoOOH) as effective active sites in the catalytic process, resulting in better OH ion capture and faster reaction kinetics.[37,38] The peaks of Nb $3d_{5/2}$ and Nb $3d_{3/2}$ are assigned to the Nb 3d spectrum of Co_2Nb_6 at 203.2 and 205.9 eV, respectively (Fig. 2c).[39] Additionally, as depicted in Fig. 2d, the fitted O 1s high-resolution spectra, and fitted peaks correspond to the Nb–O bonding (526.9 eV) and Co–O bonding (528.8 eV), respectively.[40,41] Other characterization results of Co_2Nb_6 are shown in the ESI, Fig. S1.†
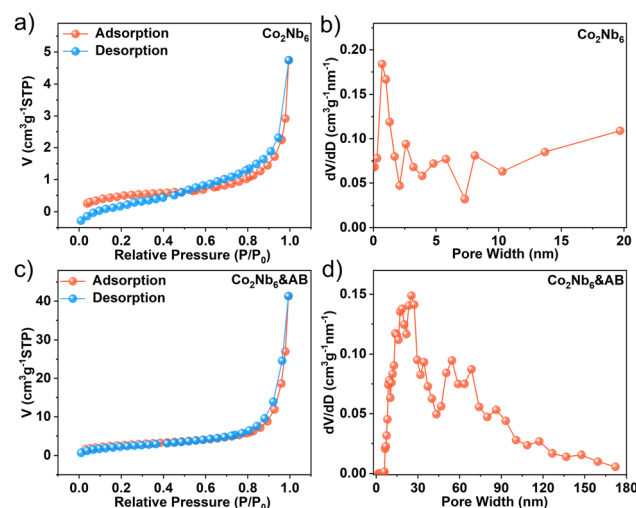
The incorporation of the "surface wetting state" concept in electrochemical reactions can be a valuable tool to improve the design of electrode surfaces for different electrochemical reactions.[42,43] Field emission scanning electron microscopy (FESEM) revealed the morphology of pristine samples. The Co_2Nb_6 shown in Fig. 3a exhibited a disordered nanostrip morphology with an average thickness of 4 μm. However, the
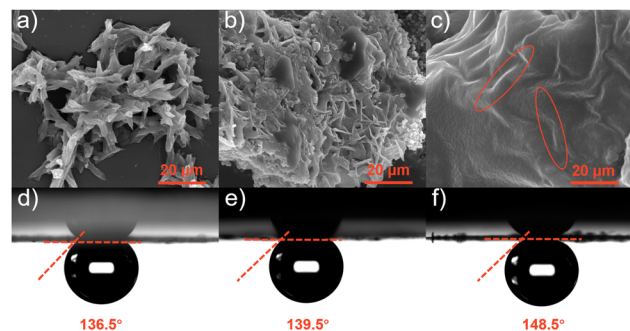
inhomogeneous particulate matter and band morphology depicted in Fig. 3b were attributed to the coexistence of Co_2Nb_6 with **AB** (Co_2Nb_6/**AB**), indicating that they were not fully cross-linked. When the PEI was added to Co_2Nb_6 and **AB** (Fig. 3c), irregularly banded material under a smooth surface was revealed, which matched the morphology of Co_2Nb_6. This indicated that in the presence of PEI, Co_2Nb_6 and **AB** were effectively adherent to one another at this time (Co_2Nb_6&**AB**), assuring the electrochemical stability of the composite.[44] Furthermore, TEM images of Co_2Nb_6&**AB** showed distinct carbon layers encapsulating the crystalline nanoparticles, further demonstrating the effective bridging of Co_2Nb_6 on **AB** *via* PEI (Fig. S2†). The elemental mapping diagram proved that the Co metal was uniformly dispersed in Co_2Nb_6&**AB** (Fig. S3†). The energy dispersive X-ray (EDX) spectrum (Fig. S4†) demonstrated that C, N, O, Co and Nb elements co-existed in Co_2Nb_6&**AB** and their specific weight distribution ratio was, respectively, about 13.34:20.56:43.33:5.48:15.29. Further analysis of the air contact angle was carried out. As shown in Fig. 3d–f, the air contact angles increased in order (136.5° < 139.5° < 148.5°) from Co_2Nb_6, Co_2Nb_6/**AB** to Co_2Nb_6&**AB**. In particular, Co_2Nb_6&**AB** was about to form a superhydrophobic surface (air contact angle ~150°), which indicated that the bubbles can be quickly detached at the electrode surface during the gas generation reaction on its surface, allowing full contact between the catalyst surface and the electrolyte and also avoiding the loss of catalyst active material by stripping due to bubble adhesion.[29,45]

The N_2 adsorption–desorption isotherms of Co_2Nb_6 and Co_2Nb_6&**AB** samples both exhibited the typical type IV curve, indicating the presence of inhomogeneous pores (Fig. 4a and c).[46] Although Co_2Nb_6 showed a very low specific surface area (1.762 m^2 g^{-1}), the pore size distribution revealed a microporous structure of less than 1 nm (Fig. 4b), which accorded

Fig. 3 (a–c) SEM images of Co_2Nb_6, Co_2Nb_6/**AB** and Co_2Nb_6&**AB**, respectively; and (d–f) air contact angles of Co_2Nb_6, Co_2Nb_6/**AB** and Co_2Nb_6&**AB**, respectively.

Fig. 4 N_2 adsorption–desorption isotherms of (a) Co_2Nb_6 and (c) Co_2Nb_6&**AB**; and pore size distribution curves for (b) Co_2Nb_6 and (d) Co_2Nb_6&**AB**.

well with the structural analysis of single crystal resolution. The bridging of acetylene black on **Co₂Nb₆** could increase the surface area of **Co₂Nb₆&AB** 8-fold (Fig. 4d) with mesopores and macroporous structures of 20–70 nm. **Co₂Nb₆** can successfully adhere to the surface of **AB**, creating pore channels for excellent electrolyte transport.[35] The relatively high surface area and rich pore structure of **Co₂Nb₆&AB** can facilitate the exposure of more active sites.[47]

Electrochemical tests

We evaluated the catalytic performance of samples for the urea oxidation reaction (UOR) using a conventional three-electrode system in alkaline media. The UOR and OER activities of **Co₂Nb₆&AB** catalysts were evaluated by linear sweep voltammetry (LSV) in an aqueous solution of 1 M KOH with 0.33 M urea. As shown in Fig. 5a, **Co₂Nb₆&AB** required a potential of 1.378 V to catalyze the UOR at 10 mA cm⁻², which was a considerable decrease of 270 mV compared to the OER (1.648 V). These results suggested that urea-assisted hydrogen production was more energy-efficient than the OER.[48] Additionally, the UOR performances of bare carbon cloth (CC), **Nb₆&AB**, CoO&AB, RuO₂ and **Co₂Nb₆&AB** were investigated under the same conditions, and the corresponding LSV curves

are shown in Fig. 5b. The electrocatalytic activity of bare CC, **Nb₆&AB** and CoO&AB was found to be very low, whereas the **Co₂Nb₆&AB** electrode demonstrated significant UOR catalytic activity that was 113 mV lower than that of the RuO₂ electrode. To provide a more intuitive comparison of the catalysts' capabilities, Fig. 5c depicts the potentials required by **Co₂Nb₆&AB**, **Nb₆&AB**, CoO&AB, and RuO₂ at various current densities. Moreover, the **Co₂Nb₆&AB** electrode exhibited a notably low Tafel slope of 58.7 mV dec⁻¹, which was lower than those of bare CC (237.7 mV dec⁻¹), **Nb₆&AB** (185.1 mV dec⁻¹), CoO&AB (148.6 mV dec⁻¹) and RuO₂ (127.4 mV dec⁻¹) electrodes (Fig. 5d). This finding suggested that the **Co₂Nb₆&AB** electrode exhibited faster UOR kinetics in practical applications. The turnover frequency (TOF) values of CoO&AB and **Co₂Nb₆&AB** are shown in Fig. S5† based on the number of metal Co sites. The TOF values of **Co₂Nb₆&AB** at different overpotentials (200 mV, 300 mV, 400 mV) were higher than those of CoO&AB, further demonstrating the higher atomic efficiency of metallic Co in **Co₂Nb₆&AB**. Remarkably, in comparison with previously reported Co-based catalysts, **Co₂Nb₆&AB** displayed excellent UOR performance (Table S3†). Meanwhile, Fig. 5e depicts the Nyquist diagram and corresponding equivalent circuit (inset), which were used to calculate the charge transfer resistance (R_{ct}) of the electrolyte/catalyst interface based on the fitted semicircle diameter. When compared to other catalysts, **Co₂Nb₆&AB** exhibited lower interfacial charge transfer resistance (the specific fitting parameters are shown in Table S4†). This result demonstrated that **Co₂Nb₆&AB** had faster charge transfer rate and better UOR kinetics.[49]

In general, the larger the electrochemically active surface area (ECSA), the more active sites are thought to be exposed, and the higher the catalytic reaction activity. The ECSA of a catalyst is evaluated by the double-layer capacitance (C_{dl}). We have calculated the C_{dl} values based on the CV plots in non-Faraday regions (Fig. S6†), and the C_{dl} value of **Co₂Nb₆&AB** was 4.75 mF cm⁻², which was higher than those of bare CC (0.90 mF cm⁻²), **Nb₆&AB** (1.15 mF cm⁻²), CoO&AB (1.69 mF cm⁻²) and RuO₂ (3.47 mF cm⁻²), suggesting that the best intrinsic catalytic activity occurs on **Co₂Nb₆&AB**. These findings demonstrated that the synergistic interaction of **AB** and **Co₂Nb₆** resulted in the UOR activity of **Co₂Nb₆&AB**. Apart from catalytic activity, long-term durability is an essential parameter to evaluate the potential of electrocatalysts for practical applications. The stability of the catalyst was evaluated by a chronopotentiometry test with a constant current density of 10 mA cm⁻². As shown in Fig. 5f, after 10 h of testing, the UOR performance of **Co₂Nb₆&AB** remained nearly stable (2 mV shift). The cyclic voltammetry measurement also displayed robust stability with negligible loss after 3000 cycles, as determined by the CV test. To verify the effective adhesion of **Co₂Nb₆** to the **AB** surface using PEI, stability test studies on **Co₂Nb₆/AB** catalysts without PEI addition were performed under the same conditions. As a comparison, the LSV curve test (Fig. S7†) and the chronopotentiometry test (Fig. S8†) were performed on the **Co₂Nb₆/AB** sample. It was evident that activity decreased significantly at the beginning of the test, which may have been
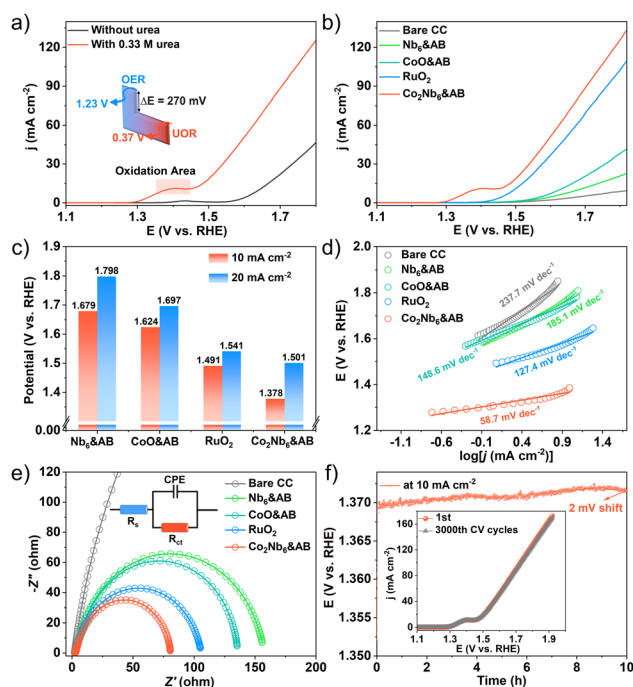
Fig. 5 Electrochemical urea oxidation performance. (a) UOR and OER performances of the **Co₂Nb₆&AB** electrode in 1.0 M KOH solution with and without 0.33 M urea at a scan rate of 5 mV·s⁻¹; (b) UOR polarization curves for bare CC, **Nb₆&AB**, CoO&AB, RuO₂, and **Co₂Nb₆&AB**; (c) comparison of potentials at 10 mA cm⁻² and 20 mA cm⁻² for the corresponding electrodes; (d) Tafel plots of the catalysts in 1 M KOH with 0.33 M urea; (e) Nyquist plots of the catalysts in 1 M KOH with 0.33 M urea (inset: Nyquist curve fitting equivalent circuit); and (f) chronoamperometric curves for **Co₂Nb₆&AB** at 10 mA cm⁻² constant current density in 1 M KOH with 0.33 M urea (inset: before and after a 3000 cycle CV scan, the LSV curves of **Co₂Nb₆&AB**).

caused by active ingredient shedding.[50] Finally, XRD analysis of sample powders before and after testing revealed that the crystal structure of the **Co₂Nb₆&AB** catalysts remained essentially intact (Fig. S9†), emphasizing the remarkable stability of the composites under alkaline oxidation conditions.

To acquire a better understanding of the urea oxidation reaction (UOR) mechanism, cyclic voltammetry (CV) was carried out. As shown in Fig. 6a, the redox peaks observed in the CV curves confirmed the presence of active sites (CoOOH) during the UOR process, which was caused by the faradaic process of Co^{3+}/Co^{2+} interconversion in the urea–alkaline electrolyte.[51] This was likely due to the fact that the Co^{3+} ion in **Co₂Nb₆&AB** was unstable in an alkaline environment and was easily reduced to $Co(OH)_2$, which was then oxidized to CoOOH in a certain voltage state. CoOOH exhibited higher electrical conductivity than crystalline materials, which was thought to be the source of electrocatalytic activity. However, the characterization of the catalytic activity of CoOOH is very challenging because CoOOH is highly soluble and the amount of catalyst is currently unknown. Furthermore, the peak areas increased steadily as the pH value increased from 12 to 14 (Fig. 6b), indicating a favorable correlation between the oxidation behavior and OH^- concentration.[52] This implied that the Co-active sites first absorbed the OH^- ion, producing the active CoOOH, and then interacted with the urea molecules. Furthermore, the Bode plot produced by contrasting frequency and phase angle revealed information about the electrochemical reaction processes. The nonhomogeneous charge distribution in the low frequency (10^{-1} Hz–10^1 Hz) region of the Bode plot was widely attributed to the generation of intermediate species on the electrode surface. According to Fig. 6c, a characteristic peak with a center frequency of approximately 10^0 Hz formed at 1.5 V in a 1 M KOH electrolyte. The peak shifted to higher frequencies and lower phase degrees as applied potentials increased,

which could be attributed to the development of the oxygen evolution reaction on the surface of the **Co₂Nb₆&AB** catalyst. This peak shifted downward roughly 300 mV lower (1.20 V) with the addition of urea due to urea oxidation at the interface, indicating that the UOR was more preferable to the OER (Fig. 6d). According to the CV data, this peak was attributed to the adsorption of OH^- by the reactive Co atom. Another peak appeared at around 1.35 V in the low-frequency range (10^0 to 10^1 Hz), which was associated with nonhomogeneous charge distributions caused by the UOR, and this was consistent with the lower onset potential given by the LSV curve above. It was worth noting that when the voltage increased, the peak frequency shifted significantly toward the higher frequency region, while the phase angle decreased greatly relative to that in the absence of urea, which may be due to the simultaneous electrolysis of water and urea.[53] These results implied that the **Co₂Nb₆&AB** catalyst improved urea dissociation kinetics and the electrooxidation of intermediates, demonstrating the catalyst's potential for promoting the UOR.
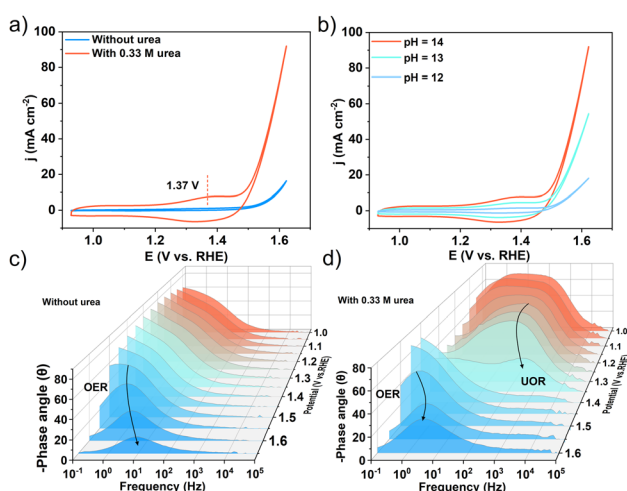
Conclusions

In this study, a facile and efficient approach was employed to synthesize **Co₂Nb₆&AB** catalyst. In particular, the **Co₂Nb₆** cluster is strategically attached to the surface of acetylene black *via* PEI. The **Co₂Nb₆&AB** catalyst exhibits outstanding performance in the urea oxidation reaction (UOR) in an alkaline electrolyte, which is found to be about 270 mV lower than that of the oxygen evolution reaction (OER) at a current density of 10 mA cm⁻². The catalyst also displays faster charge transfer rates and better UOR kinetics. Moreover, the long-term durability and stability of the catalyst in alkaline solutions are also satisfactory. These superior catalytic properties are attributed to several key factors: (i) improved conductivity of the catalyst due to the incorporation of acetylene black, which facilitates electron transport; (ii) enhanced dispersion of active sites on the surface of acetylene black *via* the use of PEI, which effectively suppresses the aggregation of Co atoms; and (iii) the exposure of abundant active sites, which accelerates charge transfer and bubble desorption.

Fig. 6 (a) CV curves of **Co₂Nb₆&AB** in 1.0 M KOH with and without 0.33 M urea at a scan rate of 5 mV s⁻¹; (b) CV curves of the **Co₂Nb₆&AB** electrocatalyst in urea–alkaline electrolytes at various pH values; Bode plots of **Co₂Nb₆&AB** in 1 M KOH without (c) and with (d) 0.33 M urea at different potentials.

Author contributions

Yan-Qiong Sun and Shou-Tian Zheng designed and led the project, revised the manuscript and acquired funding. Da-Huan Li performed material characterization and wrote the original draft. Nian Shi performed the crystal synthesis. Yong-Jiang Wang was responsible for the crystal structure determinations, and Ping-Wei Cai was responsible for electrochemical metrology analysis.

Conflicts of interest

There are no conflicts to declare.

This journal is © the Partner Organisations 2023

Inorg. Chem. Front., 2023, **10**, 4789–4796 | **4793**

References

1 F.-C. Shen, Y. Wang, Y.-J. Tang, S.-L. Li, Y.-R. Wang, L.-Z. Dong, Y.-F. Li, Y. Xu and Y.-Q. Lan, CoV_2O_6-V_2O_5 coupled with porous N-doped reduced graphene oxide composite as a highly efficient electrocatalyst for oxygen evolution, *ACS Energy Lett.*, 2017, **2**, 1327–1333.

2 L.-N. Zhang, Z.-L. Lang, Y.-H. Wang, H.-Q. Tan, H.-Y. Zang, Z.-H. Kang and Y.-G. Li, Cable-like Ru/WNO@C nanowires for simultaneous high-efficiency hydrogen evolution and low-energy consumption chlor-alkali electrolysis, *Energy Environ. Sci.*, 2019, **12**, 2569–2580.

3 W. Luo, J. Hu, H. Diao, B. Schwarz, C. Streb and Y. F. Song, Robust polyoxometalate/nickel foam composite electrodes for sustained electrochemical oxygen evolution at high pH, *Angew. Chem., Int. Ed.*, 2017, **56**, 4941–4944.

4 J. Shen, Q. Li, W. Zhang, Z. Cai, L. Cui, X. Liu and J. Liu, Spherical Co_3S_4 grown directly on Ni–Fe sulfides as a porous nanoplate array on $FeNi_3$ foam: a highly efficient and durable bifunctional catalyst for overall water splitting, *J. Mater. Chem. A*, 2022, **10**, 5442–5451.

5 S. L. Fereja, P. Li, Z. Zhang, J. Guo, Z. Fang, Z. Li, S. He and W. Chen, W-doping induced abundant active sites in a 3D NiS_2/MoO_2 heterostructure as an efficient electrocatalyst for urea oxidation and hydrogen evolution reaction, *Chem. Eng. J.*, 2022, **432**, 134274.

6 Z. Xu, Q. Chen, Q. Chen, P. Wang, J. Wang, C. Guo, X. Qiu, X. Han and J. Hao, Interface enables faster surface reconstruction in a heterostructured Co–Ni–S electrocatalyst towards efficient urea oxidation, *J. Mater. Chem. A*, 2022, **10**, 24137–24146.

7 G.-Y. He, Y.-T. Wang, X.-M. Chen, Y. Zhou, C. Meng and F.-T. Li, Laser in situ synthesis of $NiFe_2O_4$ nanoparticle-anchored NiFe(OH)$_x$ nanosheets as advanced electrocatalysts for the oxygen evolution and urea oxidation reactions, *Electrochim. Acta*, 2022, **411**, 140074.

8 Y. Wang, C. Wang, H. Shang, M. Yuan, Z. Wu, J. Li and Y. Du, Self-driven Ru-modified NiFe MOF nanosheet as multifunctional electrocatalyst for boosting water and urea electrolysis, *J. Colloid Interface Sci.*, 2022, **605**, 779–789.

9 Y. Sun and S. Chen, New electrocatalysts and mechanisms pave the way to urea oxidation with superior activities and stability, *Sci. China: Chem.*, 2021, **65**, 199–201.

10 Y. Liu, S. F. Zhao, S. X. Guo, A. M. Bond, J. Zhang, G. Zhu, C. L. Hill and Y. V. Geletii, Electrooxidation of ethanol and methanol using the molecular catalyst $[\{Ru_4O_4(OH)_2(H_2O)_4\}(\gamma\text{-}SiW_{10}O_{36})_2]^{10-}$, *J. Am. Chem. Soc.*, 2016, **138**, 2617–2628.

11 J. Gautam, Y. Liu, J. Gu, Z. Ma, J. Zha, B. Dahal, L. N. Zhang, A. N. Chishti, L. Ni, G. Diao and Y. Wei, Fabrication of polyoxometalate anchored zinc cobalt sulfide nanowires as a remarkable bifunctional electrocatalyst for overall water splitting, *Adv. Funct. Mater.*, 2021, **31**, 2106147.

12 P. Balasubramanian, A. Jansirani, S.-B. He, H.-H. Deng, H.-P. Peng, X.-H. Xia and W. Chen, Rational construction of N,S-doped carbon wrapped $MnFe_2O_4$ nanospheres with copious oxygen deficiency as extremely efficient and robust electrocatalyst for urea electrocatalysis, *J. Power Sources*, 2021, **494**, 229757.

13 Y. Jiang, S. Gao, J. Liu, G. Xu, Q. Jia, F. Chen and X. Song, Ti-Mesh supported porous CoS_2 nanosheet self-interconnected networks with high oxidation states for efficient hydrogen production via urea electrolysis, *Nanoscale*, 2020, **12**, 11573–11581.

14 Z. Cao, H. Mao, X. Guo, D. Sun, Z. Sun, B. Wang, Y. Zhang and X.-M. Song, Hierarchical Ni(OH)$_2$/polypyrrole/graphene oxide nanosheets as excellent electrocatalysts for the oxidation of urea, *ACS Sustainable Chem. Eng.*, 2018, **6**, 15570–15581.

15 J. Wang, Z. Zhao, C. Shen, H. Liu, X. Pang, M. Gao, J. Mu, F. Cao and G. Li, Ni/NiO heterostructures encapsulated in oxygen-doped graphene as multifunctional electrocatalysts for the HER, UOR and HMF oxidation reaction, *Catal. Sci. Technol.*, 2021, **11**, 2480–2490.

16 H. Liu, S. Zhu, Z. Cui, Z. Li, S. Wu and Y. Liang, Ni_2P nanoflakes for the high-performing urea oxidation reaction: linking active sites to a UOR mechanism, *Nanoscale*, 2021, **13**, 1759–1769.

17 B. Zhu, Z. Liang and R. Zou, Designing advanced catalysts for energy conversion based on urea oxidation reaction, *Small*, 2020, **16**, e1906133.

18 J. Lei, X. X. Fan, T. Liu, P. Xu, Q. Hou, K. Li, R. M. Yuan, M. S. Zheng, Q. F. Dong and J. J. Chen, Single-dispersed polyoxometalate clusters embedded on multilayer graphene as a bifunctional electrocatalyst for efficient Li-S batteries, *Nat. Commun.*, 2022, **13**, 202.

19 A. Joshi, P. Sood, A. Gaur, D. Rani, V. Madaan and M. Singh, Improved OER performance of an Anderson-supported cobalt coordination polymer by assembling with acetylene black, *J. Mater. Chem. A*, 2022, **10**, 12805–12810.

20 N. Shi, Y.-J. Wang, X.-X. Li, Y.-Q. Sun and S.-T. Zheng, An inorganic Co-containing heteropolyoxoniobate: reversible chemochromism and H_2O-dependent proton conductivity properties, *Inorg. Chem. Front.*, 2021, **8**, 5225–5233.

21 Y. D. Lin, Z. K. Zhu, R. Ge, H. Yu, Z. Li, C. Sun, Y. Q. Sun, X. X. Li and S. T. Zheng, Proton conductive polyoxoniobate frameworks constructed from nanoscale $\{Nb_{68}O_{200}\}$ cages, *Chem. Commun.*, 2021, **57**, 4702–4705.

22 H.-Y. Zhao, Y.-Z. Li, J.-W. Zhao, L. Wang and G.-Y. Yang, State-of-the-art advances in the structural diversities and catalytic applications of polyoxoniobate-based materials, *Coord. Chem. Rev.*, 2021, **443**, 213966.

23 X. Ma, Y. Bian, Y. Zhou, Q. Zhao, Y. Tian, J. Hua and P. Ma, Synthesis, characterization, and catalytic property of a hybrid nanoscale polyoxoniobate, *J. Cluster Sci.*, 2020, **32**, 613–620.

24 J. H. Son, J. Wang and W. H. Casey, Structure, stability and photocatalytic H_2 production by Cr-, Mn-, Fe-, Co-, and Ni-substituted decaniobate clusters, *Dalton Trans.*, 2014, **43**, 17928–17933.

25 R. Gong, D. Gao, R. Liu, D. Sorsche, J. Biskupek, U. Kaiser, S. Rau and C. Streb, Self-activation of a polyoxometalate-derived composite electrocatalyst for the oxygen evolution reaction, *ACS Appl. Energy Mater.*, 2021, **4**, 12671–12676.

26 J. Hu, Y. Wang, X. Zhang, Y. Chi, S. Yang, J. Li and C. Hu, Controllable assembly of vanadium-containing polyoxoniobate-based three-dimensional organic-inorganic hybrid compounds and their photocatalytic properties, *Inorg. Chem.*, 2016, **55**, 7501–7507.

27 Y.-L. Wu, Y.-Q. Sun, X.-X. Li and S.-T. Zheng, A new dimeric isopolyoxoniobate $\{\beta,-H_4Nb_{52}O_{150}\}$ decorated with copper (II)-ethylenediamine for hydrolytic decomposition of chemical warfare agent simulant DMMP, *Inorg. Chem. Commun.*, 2020, **113**, 107815.

28 L. Guo, L. He, Q. Zhuang, B. Li, C. Wang, Y. Lv, J. Chu and Y. F. Song, Recent advances in confining polyoxometalates and the applications, *Small*, 2023, 2207315.

29 M. Bae, Y. Kang, D. W. Lee, D. Jeon and J. Ryu, Superaerophobic polyethyleneimine hydrogels for improving electrochemical hydrogen production by promoting bubble detachment, *Adv. Energy Mater.*, 2022, **12**, 2201452.

30 X. Yin, Z. Zhang, K. Yao, X. Xu and Y. Wang, Hydrophobic POM electrocatalyst achieves low voltage "charge" in Zn-Air battery coupled with bisphenol a degradation, *Chem. – Eur. J.*, 2021, **27**, 8774–8781.

31 Y. Zheng, P. Tang, X. Xu and X. Sang, POM derived UOR and HER bifunctional NiS/MoS_2 composite for overall water splitting, *J. Solid State Chem.*, 2020, **292**, 121644.

32 Z. Zeb, Y. Huang, L. Chen, W. Zhou, M. Liao, Y. Jiang, H. Li, L. Wang, L. Wang, H. Wang, T. Wei, D. Zang, Z. Fan and Y. Wei, Comprehensive overview of polyoxometalates for electrocatalytic hydrogen evolution reaction, *Coord. Chem. Rev.*, 2023, **482**, 215058.

33 Y.-Y. Ma, C.-X. Wu, X.-J. Feng, H.-Q. Tan, L.-K. Yan, Y. Liu, Z.-H. Kang, E.-B. Wang and Y.-G. Li, Highly efficient hydrogen evolution from seawater by a low-cost and stable CoMoP@C electrocatalyst superior to Pt/C, *Energy Environ. Sci.*, 2017, **10**, 788–798.

34 N. Li, J. Liu, B.-X. Dong and Y.-Q. Lan, Polyoxometalate-based compounds for photo- and electrocatalytic applications, *Angew. Chem., Int. Ed.*, 2020, **59**, 20779–20793.

35 Y. Shimoyama, N. Ogiwara, Z. Weng and S. Uchida, Oxygen evolution reaction driven by charge transfer from a Cr complex to Co-containing polyoxometalate in a porous Ionic prystal, *J. Am. Chem. Soc.*, 2022, **144**, 2980–2986.

36 X. Yang, J. Chen, W. Yang, H. Lina and X. Luo, Influence of Zn and Co co-doping on oxygen evolution reaction electro-

37 X. Du, Y. Ding and X. Zhang, MOF-derived Zn–Co–Ni sulfides with hollow nanosword arrays for high-efficiency overall water and urea electrolysis, *Green Energy Environ.*, 2023, **8**, 798–811.

38 R. Jia, M. Xia, L. Tang, L. Yu, Y. Yang, Y. Zhang, X. Bo, S. Zhou, Y. Tu and D. Deng, Single-atomic Ir and Mo Co-confined in a Co layered hydroxide nanobox mutually boost oxygen evolution, *ACS Catal.*, 2022, **12**, 13513–13522.

39 Y. Gao, L. Qi, F. He, Y. Xue and Y. Li, Selectively growing a highly active Interface of mixed Nb-Rh oxide/2D carbon for electrocatalytic hydrogen production, *Adv. Sci.*, 2022, **9**, e2104706.

40 X. H. Chen, X. L. Li, L. L. Wu, H. C. Fu, J. Luo, L. Shen, Q. Zhang, J. L. Lei, H. Q. Luo and N. B. Li, Nb_2O_5−Ni_3N heterojunction tuned by interface oxygen vacancy engineering for the enhancement of electrocatalytic hydrogen evolution activity, *J. Mater. Chem. A*, 2021, **9**, 11563–11570.

41 M. Pan, W. Chen, G. Qian, T. Yu, Z. Wang, L. Luo and S. Yin, Carbon-encapsulated Co3V decorated Co_2VO_4 nanosheets for enhanced urea oxidation and hydrogen evolution reaction, *Electrochim. Acta*, 2022, **407**, 139882.

42 A. Angulo, P. van der Linde, H. Gardeniers, M. Modestino and D. F. Rivas, Influence of bubbles on the energy conversion efficiency of electrochemical reactors, *Joule*, 2020, **4**, 555–579.

43 Y. Li, H. Zhang, T. Xu, Z. Lu, X. Wu, P. Wan, X. Sun and L. Jiang, Under-water superaerophobic pine-shaped Pt nanoarray electrode for ultrahigh-performance hydrogen evolution, *Adv. Funct. Mater.*, 2015, **25**, 1737–1744.

44 D. Jeon, H. Kim, C. Lee, Y. Han, M. Gu, B. S. Kim and J. Ryu, Layer-by-layer assembly of polyoxometalates for photoelectrochemical (PEC) water splitting: toward modular PEC devices, *ACS Appl. Mater. Interfaces*, 2017, **9**, 40151–40161.

45 J. Zhang, F. Dong, C. Wang, J. Wang, L. Jiang and C. Yu, Integrated bundle electrode with wettability-gradient copper cones Inducing continuous generation, directional transport, and efficient collection of H_2 bubbles, *ACS Appl. Mater. Interfaces*, 2021, **13**, 32435–32441.

46 D. C. Nguyen, T. L. L. Doan, S. Prabhakaran, D. T. Tran, D. H. Kim, J. H. Lee and N. H. Kim, Hierarchical Co and Nb dual-doped MoS_2 nanosheets shelled micro-TiO_2 hollow spheres as effective multifunctional electrocatalysts for HER, OER, and ORR, *Nano Energy*, 2021, **82**, 105750.

47 D. Li, Y. Qu, S. Li, M. Wei and Y. Liu, A novel honeycomb Fe-N-C composition derived from wheat flour as an efficiency catalyst for the oxygen reduction reaction, *J. Solid State Electrochem.*, 2020, **24**, 1105–1112.

48 Z.-Y. Yu, C.-C. Lang, M.-R. Gao, Y. Chen, Q.-Q. Fu, Y. Duan and S.-H. Yu, Ni–Mo–O nanorod-derived composite catalysts for efficient alkaline water-to-hydrogen conversion via urea electrolysis, *Energy Environ. Sci.*, 2018, **11**, 1890–1897.

49 H. Xu, K. Ye, K. Zhu, Y. Gao, J. Yin, J. Yan, G. Wang and D. Cao, Hollow bimetallic selenide derived from a

catalysis at MOF-derived, *Inorg. Chem. Front.*, 2019, **6**, 3475–3481.

This journal is © the Partner Organisations 2023

Inorg. Chem. Front., 2023, **10**, 4789–4796 | **4795**

hierarchical MOF-based Prussian blue analogue for urea electrolysis, *Inorg. Chem. Front.*, 2021, **8**, 2788–2797.

50 A. Kumar, X. Liu, J. Lee, B. Debnath, A. R. Jadhav, X. Shao, V. Q. Bui, Y. Hwang, Y. Liu, M. G. Kim and H. Lee, Discovering ultrahigh loading of single-metal-atoms via surface tensile-strain for unprecedented urea electrolysis, *Energy Environ. Sci.*, 2021, **14**, 6494–6505.

51 W. Yuan, T. Jiang, X. Fang, Y. Fan, S. Qian, Y. Gao, N. Cheng, H. Xue and J. Tian, Interface engineering of S-doped $Co_2P@Ni_2P$ core–shell heterostructures for

efficient and energy-saving water splitting, *Chem. Eng. J.*, 2022, **439**, 135743.

52 K. Zhang, C. Liu, N. Graham, G. Zhang and W. Yu, Modulation of dual centers on cobalt-molybdenum oxides featuring synergistic effect of intermediate activation and radical mediator for electrocatalytic urea splitting, *Nano Energy*, 2021, **87**, 106217.

53 H. Qin, Y. Ye, J. Li, W. Jia, S. Zheng, X. Cao, G. Lin and L. Jiao, Synergistic engineering of doping and vacancy in $Ni(OH)_2$ to boost urea electrooxidation, *Adv. Funct. Mater.*, 2022, **33**, 2209698.

4796 | *Inorg. Chem. Front.*, 2023, **10**, 4789–4796

This journal is © the Partner Organisations 2023